OMAE2018-77590

DYNAMIC RESPONSE ANALYSIS OF A FLOATING BRIDGE SUBJECTED TO ENVIRONMENTAL LOADS

Zhengshun Cheng *

Department of Marine Technology
CeSOS and AMOS
Norwegian University of Science and Technology
Trondheim, 7491, Norway
Email: zhengshun.cheng@ntnu.no

Zhen Gao

Department of Marine Technology
CeSOS and AMOS
NTNU
Trondheim, 7491, Norway
Email: zhen.gao@ntnu.no

Torgeir Moan

Department of Marine Technology
CeSOS and AMOS
NTNU
Trondheim, 7491, Norway
Email: torgeir.moan@ntnu.no

ABSTRACT

Designing floating bridges for wide and deep fjords is very challenging. The floating bridge is subjected to wind, wave, and current loads. All these loads and corresponding load effects should be properly evaluated, e.g. for ultimate limit state design check. In this study, the wind-, wave- and current-induced load effects of an end-anchored floating bridge are numerically investigated. The considered floating bridge, about 4600 m long, was an early concept for crossing Bjørnafjorden, Norway. It consists of a cable-stayed high bridge part and a pontoon-supported low bridge part, and has a number of eigen-modes, which might be excited by the relevant environmental loads. Numerical simulations show that the sway motion and strong axis bending moment along the bridge girder are primarily induced by wind loads, while variations of heave motion and weak axis bending moment are mainly induced by wave loads. Current loads mainly provide damping force to reduce the variations of sway motion and strong axis bending moment. Turbulent wind can cause significantly larger low-frequency resonant responses than second-order difference-frequency wave loads.

INTRODUCTION

The Norwegian Public Roads Administration (NPRA) has a long-term goal to build a repaired and ferry-free Coastal Highway E39, which will halve travel time between Kristiansand and Trondheim. Several wide and deep fjords on the west coast of Norway are to be connected by floating bridges, instead of ferries. Designing of floating bridges for wide and deep fjords is very challenging. One of the challenges comes from the complex environment condition in fjords, including wind, wave and current. The dynamic behavior of a very long floating bridge subjected to wind, wave and current loads is very complex and requires cautious modeling and assessment.

A review of worldwide development of floating bridges was given in [1]. There are currently a limited number of floating bridges, such as the Hood Canal bridge in the United States [2], the Bergsøysund bridge [3] and the Nordhordland bridge [4] in Norway, and the Yumemai bridge [5] in Japan, etc. The existing floating bridges are mainly supported by pontoons.

Dynamic behavior of pontoon-type floating bridges due to wave loads have been studied by many researchers. In 1989 Løken et al. [7] conducted a numerical and experimental study of a pontoon type floating bridge under long-crested and short-crested waves. Numerical results based on potential flow theory presented fairly good agreements with those from the model test. Seif and Inoue [8] proposed a unified method for the analysis of a discrete pontoon floating bridge that takes into account complete hydrodynamic interaction between the pontoons. Kvåle et al. [3] developed a frequency domain method to account for the hydroelastic responses of pontoon type floating bridges, and applied it to investigate the dynamic behavior of the Bergsøysund bridge. Fu et al. [9] proposed a time-domain method for hydroelastic
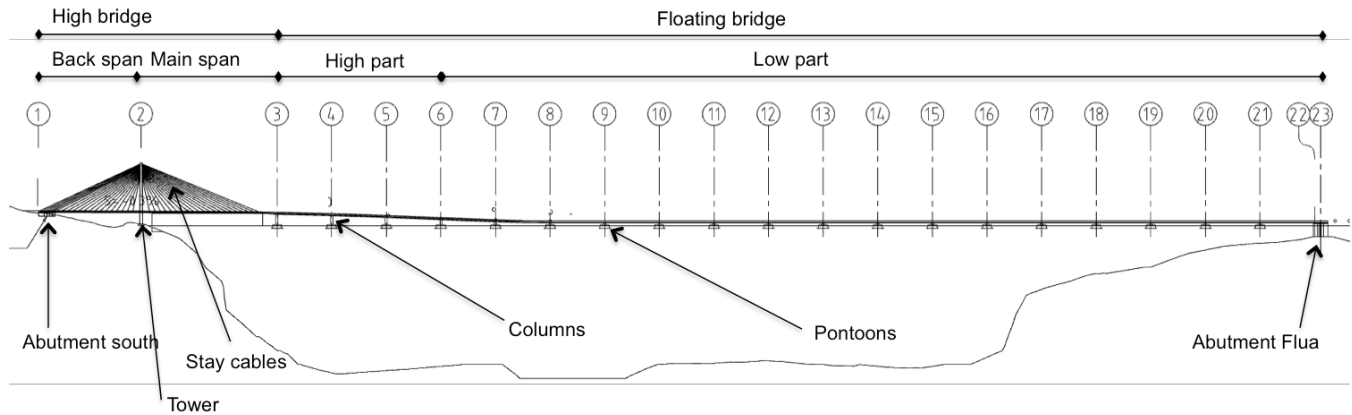
---

* Address all correspondence to this author.

FIGURE 1. Overview of the end anchored curved floating bridge concept [6].

analysis of floating bridges based on multi-rigid-body connected by elastic beams.

Compared to wave loads, wind loads and load effects on pontoon-type floating bridges are much less addressed in the literature. Lie et al. [10] investigated the feasibility of deploying an end-anchored floating bridge in Masfjorden and compared its dynamic response with a submerged tube bridge concept. The wind, wave and current loads on the floating bridges were considered; however, the modeling of wind, wave and current loads were not well stated. Sha et al. [11] studied the dynamic responses of an end-anchored floating bridge under wind and wave loads, in which long-crested wave loads were considered.

This study addresses the dynamic responses of an end-anchored curved floating bridge subjected to wind, wave and current loads. The considered floating bridge consists of a cable-stayed high bridge part and a pontoon-supported low bridge part. Modeling of wave-induced loads of the considered floating bridge was extensively studied in [12], and wave load effects of this floating bridge were also investigated in homogeneous and inhomogeneous waves [12, 13]. In this paper, the wind-, wave-, and current-induced load effects on the floating bridge are compared and their relative importances are revealed. A more comprehensive study on the modeling and dynamic response analysis of the floating bridge subjected to wind, wave and current loads is addressed in [14].

FLOATING BRIDGE CONCEPT

This study considers an end-anchored curved floating bridge, which was an early concept for crossing Bjørnafjorden. Fig. 1 gives an overview of the whole bridge, in which key structures are marked. The floating bridge is approximately 4600 m long, and is curved in the horizontal plane with a radius of about 5000 m. It consists of a high bridge part and a low bridge part. The high bridge, designed for ship navigation, is cable-stayed lo-

cated in South. It has a main span of 490 m and a back span of 370 m. A total of 80 cables are used to carry the girder. The low bridge part is supported by 19 pontoons with a span of about 197 m. The bridge girder is supported by the pontoons through columns.

FLOATING BRIDGE MODEL

A numerical model of the floating bridge, as shown in Fig. 2, has been built using the codes SIMO/RIFLEX [12]. This section only gives a brief description of key features of the numerical model. Detailed information is given in [12].

SIMO [15] accounts for the hydrodynamic loads acting on the pontoons. Modeling of wave loads are described in detail in the next section. RIFLEX [16] is a nonlinear finite element solver. It represents the girder, tower, columns and cables as nonlinear flexible elements, while the pontoons are modeled as rigid bodies. It should be noted that in the original design, the bridge girder consists of two parallel steel boxes connected by crossbeams, while in the numerical model, it is simplified as an equivalent beam. The detailed properties of the bridge girder, columns, cables and tower are described in [12] and [6] and are not presented here. Aerodynamic loads acting on structures are accounted for in RIFLEX.

In the numerical model, two ends of the bridge and the tower bottom are fixed. The connection point between the girder and the tower has fixed degree of freedom in transverse direction (sway). Master-slave rigid connection is applied between cable ends and girder, between girder and columns, and between pontoons and columns. The pretension in each cable is also considered in the numerical model.

The global coordinate system is defined as shown in Fig. 3. X is positive in the north direction, and Y is positive in the west direction. and Z is positive upward. The origin is located at the water plane and is 2250 m North of the south end. The incoming
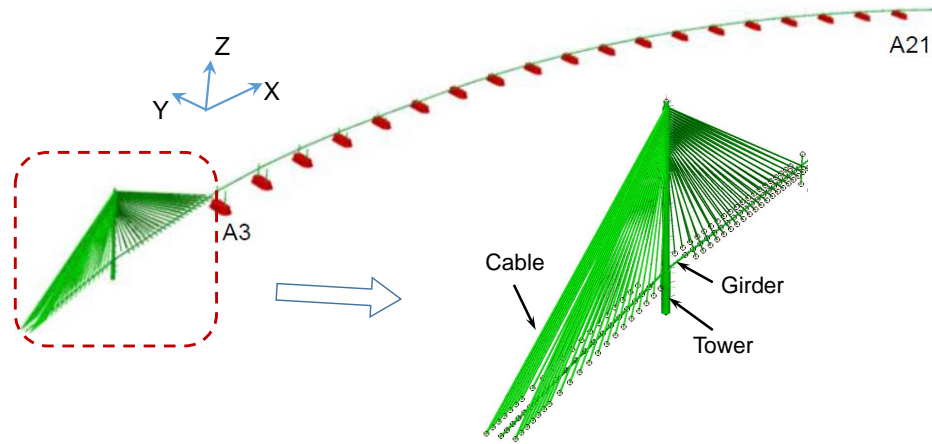
FIGURE 2. The end anchored curved floating bridge model including a cable stayed high bridge and a pontoon supported low bridge [12].
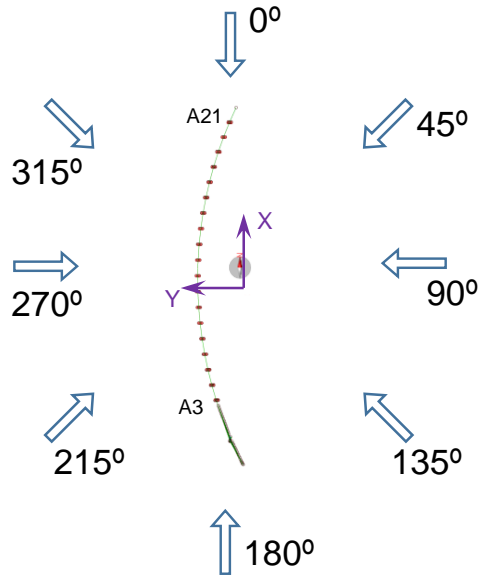

FIGURE 3. Definition of the global coordinate system. Directions of incoming wind, wave and current are also marked. Note that the fjord boundary condition is not plotted here.

FIGURE 4. Definition of rigid body motions of the pontoons and the strong and weak axes of the bridge girder [17].

TABLE 1. The first four eigen periods of the floating bridge model. The definition of "X" and "Y" motions are shown in Fig. 3. "T" denotes torsion.

Mode	Period [6]	Frequency [6]	Period	Error	Dominant motions	
	[s]	[rad/s]	[s]	[%]	Primary motion	Secondary motion
1	56.72	0.111	55.52	2.12	Y	X
2	31.69	0.199	31.81	-0.38	Y	X
3	22.68	0.277	23.07	-1.72	Y	T
4	18.62	0.337	19.04	-2.26	Y	X

directions of wind, wave and current are also indicated in Fig. 3. The definitions of rigid body motions of the pontoons are shown in Fig. 4. The strong axis and weak axis of the bridge girder is also highlighted in Fig. 4.

Eigen-frequencies and eigen-modes for this floating bridge was analyzed in [12]. A large number of eigen-modes were identified. Table 1 gives the first four eigen-periods of the floating bridge. The corresponding eigen-modes are dominated by horizontal motions, and they are likely to be excited by second ord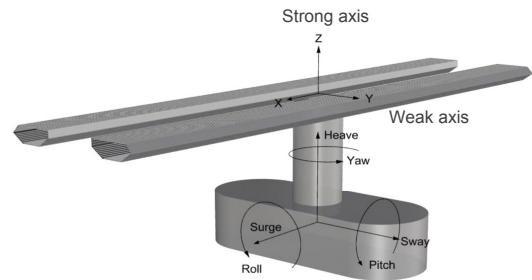er difference frequency wave loads and by low-frequency turbulent wind loads. The third mode is a combination of horizontal motion and torsional motion. In addition, there are about 20 eigen-modes that are dominated by vertical motions. They have a eigen-period ranging from 7.47 s to 11.48 s, which are due to heave motion of pontoons. More than 25 eigen-modes have a eigen-period below 3.7 s, in which the dominating motions are mainly pendulum motions, because of surge motion of pontoons.
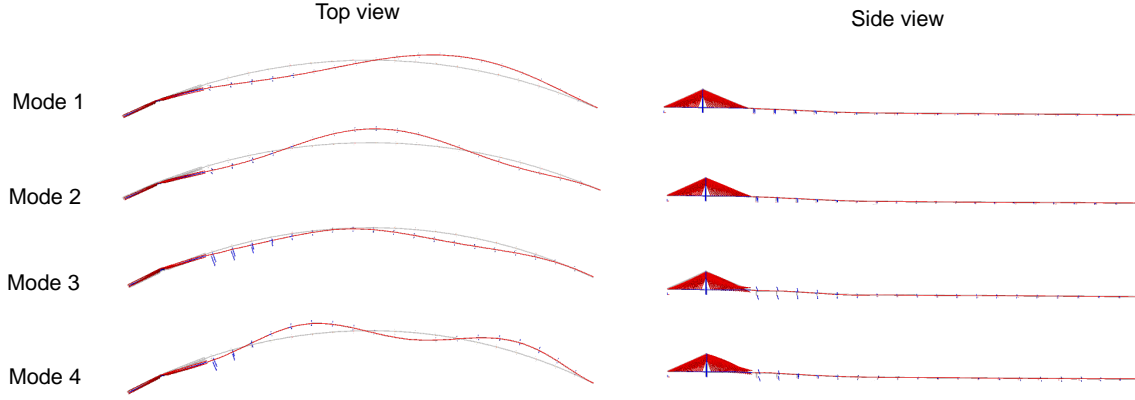
FIGURE 5. Several selected eigen-modes of the floating bridge based on eigen-value analysis by the SIMO/RIFLEX codes [12].

ENVIRONMENTAL CONDITIONS

The environmental condition considered in this study is assumed to be homogeneous and determined according to the metocean design basis for Bjørnafjorden [18]. Here only wind, wave, and current conditions with a return period of 100 years are considered.

Wave

The wave conditions in Bjørnafjorden have been thoroughly described by Cheng et al. [12]. Waves in a fjord are short-crested and short-crested waves play an important role in the dynamic responses of the floating bridge. Hence directional wave spectrum is considered in the present study and is given by

$$S_\zeta(\omega, \theta) = S(\omega)D(\theta) \qquad (1)$$

where the wave spectrum $S(\omega)$ is modeled by the JONSWAP spectrum and the directional distribution $D(\theta)$ takes the cos-n distribution as follows:

$$D(\theta) = \frac{\Gamma(1+n/2)}{\sqrt{\pi}\Gamma(1/2+n/2)} \cos^n(\theta - \theta_p) \qquad (2)$$

where n is the spreading exponent, and is set to be 4 for short crested waves [18] in this study. θ_p is the main wave direction and $|\theta - \theta_p| \le \pi/2$.

The 100-year wave conditions in Bjørnafjorden were estimated by numerical simulations, based on hindcast wind data from 1979 to 2015 [19]. Table 2 gives the 100-year wave conditions. The directional wave spectrum for the 100-year waves coming from west (270°) is shown in Fig. 6.

TABLE 2. 100-year wind waves in Bjørnafjorden [18]

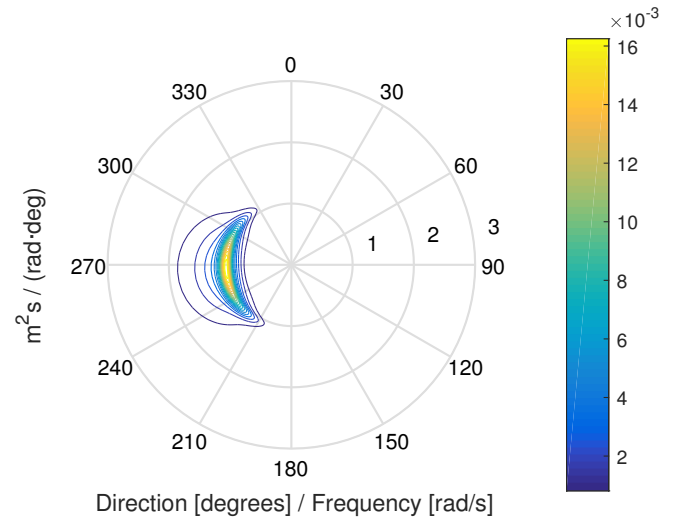| Sectors	H_s [m]	T_p [s]
345° - 75°	1.5	5.0
75° - 105°	2.8	6.6
105° - 165°	1.6	5.3
165° - 225°	1.9	5.3
225° - 315°	2.4	5.9
315° - 345°	2.5	6.2

FIGURE 6. Directional wave spectrum for waves coming from west (270°) with a significant wave height $H_s = 2.4m$, peak period $T_p = 5.9s$, and spreading exponent $n = 4$.

Wind

The 1-hour mean wind speed at 10 m height with a return period of 100 years is about 31 m/s. This is applicable for wind

coming from west (270°).

The power law formulation of wind shear is applied to describe the vertical distribution of mean wind speed. At height z above mean sea level (MSL), the mean wind speed $V_w(z)$ is determined by

$$V_w(z) = V_{wref} \left(\frac{z}{z_{ref}} \right)^{\alpha} \quad (3)$$

in which the reference height z_{ref} is chosen to be 10 m. α is the power law exponent. For wind coming from west (270°), α is approximate 0.12 for height ranging from 10 m to 60 m, and 0.14 for height ranging from 60 m to 200 m. Since the wind loads on the floating low bridge is dominating, α is chosen to be 0.12 for simplicity.

The turbulence intensity for wind coming from west (270°) is about 14%. In the numerical simulation, the 3D turbulent wind field is generated by the TurbSim [20] based on the IEC Kaimal spectral model. The corresponding coherence is also described in [20], which only considers the coherence for the horizontal component of the wind speed.

Current

The current can be assumed to go in or out the fjord, i.e. in 90° or 270°. The current velocity at different depth is given in Table 3. The current velocity profile can be determined by linear interpolation between depths according to Table 3.

TABLE 3. 100-year current profile

Depth [m]	U_c [m/s]
0-5	1.4
15	0.95
25	0.6
50	0.55
100	0.3

MODELING OF ENVIRONMENTAL LOADS
Wave and current loads

The hydrodynamic modeling of wave loads for the floating bridge has been comprehensively addressed in [12]. The pontoons are regarded as large volume structures, their hydrodynamic coefficients, such as added masses, radiation dampings, and transfer functions of wave excitation forces, etc., are first estimated based on the potential flow theory [21]. The hydrodynamic interaction between adjacent pontoons are not considered, since the spacing between adjacent pontoons are more than

4 times the typical wave length under 100-year wave condition. The wall effect due to fjord sides on the hydrodynamic coefficients is not considered either.

The added masses and radiation dampings are then applied as radiation forces in time domain using the convolution technique [22]. Regarding the wave excitation forces, this study accounts for both first order wave loads and second order difference frequency wave loads. The second order wave loads are considered by using Newman's approximation, in which only forces in surge and sway and moment in yaw are considered. Detailed descriptions of modeling of wave loads can be found in [12].

The viscous drag forces on the pontoons are incorporated through the Morison's equation by considering only the quadratic viscous drag term. They are caused by the wave kinematics, current velocity and floater velocity. The transverse viscous force per unit length is given by

$$d\mathbf{F}_{Drag}^{wa}(t) = \frac{1}{2}\rho_w \mathbf{C}_d^{wa} D(\mathbf{u}_w + \mathbf{u}_c - \mathbf{u}_b)|\mathbf{u}_w + \mathbf{u}_c - \mathbf{u}_b| \quad (4)$$

where ρ_w is the water density, $\mathbf{u}_w$ is the wave particle velocity, $\mathbf{u}_b$ is the local body velocity, $\mathbf{u}_c$ is the current velocity, D is the characteristic width of the body, and $\mathbf{C}_d^{wa}$ is the quadratic drag coefficient. The drag coefficient used in this study is $C_{dx}^{wa} = 1$, $C_{dy}^{wa} = 0.4$, and $C_{dz}^{wa} = 4.8$ [23], the corresponding coordinate system is shown in Fig. 3.

Wind loads

Structures above the MSL are subjected to wind loads under wind conditions. In the present study, the relative velocity between the wind and structures is accounted for when estimating the wind loads. The column, tower and cables are mainly subjected to viscous drag forces. The transverse viscous drag forces per unit length due to winds is given by

$$d\mathbf{F}_{Drag}^{wi}(t) = \frac{1}{2}\rho_a \mathbf{C}_d^{wi} D(\mathbf{V}_w - \mathbf{v}_b)^2 \quad (5)$$

where ρ_a is the air density, $\mathbf{V}_w$ is the wind velocity, $\mathbf{v}_b$ is the local body velocity D is the characteristic width of the body, and $\mathbf{C}_d^{wi}$ is the quadratic drag coefficient.

The wind load acting on the bridge girder is more complicated than those acting on the column, tower and cables. It usually consists of three parts: the mean force due to mean wind velocity, the buffeting force due to fluctuating wind velocity, and the frequency-dependent force induced by girder motion [24]. In this study, the frequency-dependent aerodynamic forces induced by motion of the structures are neglected. Only the mean force and buffeting force are considered. The instantaneous cross sectional drag and lift forces and moment per unit length are given

by [24]

$$\begin{bmatrix} dF_{Lift}^{wi}(t) \\ dF_{Drag}^{wi}(t) \\ dF_{Mom}^{wi}(t) \end{bmatrix} = \frac{1}{2}\rho_a D(\mathbf{V}_w - \mathbf{v}_b)^2 \begin{bmatrix} \frac{B}{D}C_l^{wi}(\alpha) \\ C_d^{wi}(\alpha) \\ \frac{B^2}{D}C_m^{wi}(\alpha) \end{bmatrix} \quad (6)$$

where B and D are the height and width of the girder, respectively. $C_l^{wi}(\alpha)$, $C_d^{wi}(\alpha)$ and $C_m^{wi}(\alpha)$ are nonlinear load coefficients. They are a function of angle of incidence α, and can be approximated by [24]

$$\begin{bmatrix} C_l^{wi}(\alpha) \\ C_d^{wi}(\alpha) \\ C_m^{wi}(\alpha) \end{bmatrix} = \begin{bmatrix} C_l^{wi}(\bar{\alpha}) \\ C_d^{wi}(\bar{\alpha}) \\ C_m^{wi}(\bar{\alpha}) \end{bmatrix} + \alpha_f \begin{bmatrix} \frac{d}{d\alpha}C_l^{wi}(\bar{\alpha}) \\ \frac{d}{d\alpha}C_d^{wi}(\bar{\alpha}) \\ \frac{d}{d\alpha}C_m^{wi}(\bar{\alpha}) \end{bmatrix} \quad (7)$$

where $\bar{\alpha}$ and α_f are the mean value and the fluctuating part of the angle of incidence. $C_l^{wi}(\bar{\alpha})$, $C_d^{wi}(\bar{\alpha})$, $C_m^{wi}(\bar{\alpha})$ are the lift, drag and moment coefficients at $\bar{\alpha}$. $\frac{d}{d\alpha}C_l^{wi}(\bar{\alpha})$, $\frac{d}{d\alpha}C_d^{wi}(\bar{\alpha})$, and $\frac{d}{d\alpha}C_m^{wi}(\bar{\alpha})$ are the slope of load coefficients at $\bar{\alpha}$. Relevant values for these parameters are given in [6] for the bridge girder considered.

The present study models the bridge girder as an airfoil in RIFLEX, and a look-up table of force coefficients as a function of angle of attack is created based on Eqs. 6 and 7.

LOAD CASES

A series of load cases (LCs) are defined in this study. LC1 only considers steady winds while LC2 only considers turbulent winds. LC3 only considers short crested wave conditions. Combination of wind and wave conditions are addressed in LC4 and LC5. LC6 considers turbulent wind, irregular waves and current. It should be noted that the wind, waves and current are assumed to be directionally aligned. Here only one direction ($270°$) is considered. For each LC (except LC1), 5 identical and independent simulations are carried out. It is used to reduce the stochastic variation of dynamic responses. The statistical values and spectra presented in the following sections are based on the average of 5 seeds for each LC.

TABLE 4. Load cases for numerical simulations

| Dir. [°] | Wave | | | Wind | | Current |
	H_s [m]	T_p [s]	Spreading (n)	U_w [m/s]	T_I	
LC1	270	-	-	-	31	0	No
LC2	270	-	-	-	31	0.14	No
LC3	270	2.4	5.9	4	0	0	No
LC4	270	2.4	5.9	4	31	0	No
LC5	270	2.4	5.9	4	31	0.14	No
LC6	270	2.4	5.9	4	31	0.14	Yes

RESULTS AND DISCUSSIONS
Representative time series

Numerical simulations under the six load cases given in Table 4 are conducted. Representative time series of simulated responses are first presented in this section to provide a overall effect of different environmental loads. Fig. 7 shows a comparison of time histories of weak axis bending moment at A6 under different combination of environmental loads. The weak axis bending moment are representative responses due to vertical motion of the bridge girder. All cases have very close mean value with respect to weak axis bending moment. The variations of different responses under different LCs are to some extent different. Therefore, the effect of environmental loads on the mean value and variation of various responses should be addressed separately.
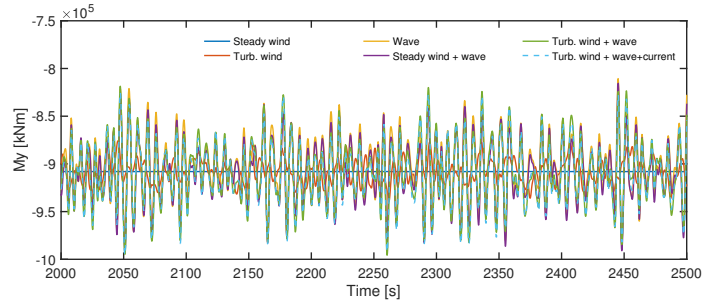

FIGURE 7. A comparison of time history of weak axis bending moment M_y at A6 under different combination of environmental loads.

Statistical analysis of dynamic responses

The mean values of sway motion and strong axis bending moment along the bridge girder under different LCs are shown in Fig. 8. In general, the cases with wind (LC1, LC2, LC4, LC5, LC6) and the case with waves only (LC3) differ greatly. The cases with wind gives rise to a much larger mean sway motion than the case with waves only, especially in the middle part of the bridge. The mean values of strong axis bending moment of the cases with wind are also larger than that of the case with waves only, at parts close to two ends of the floating bridge.

Within the cases with wind, LC1 with steady wind gives a slightly smaller mean value in sway than LC2, LC4, and LC5. LC6 with turbulent wind, waves and current gives relatively larger mean value of sway motion than LC5 with turbulent wind and waves, which is due to current loads acting on the pontoons. However, the cases with wind have very close mean value of strong axis bending moment, indicating that the strong axis bending moment is not sensitive to wave and current loads when then bridge is subjected to wind loads.
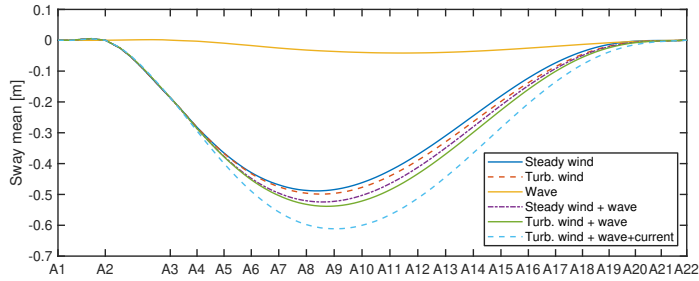
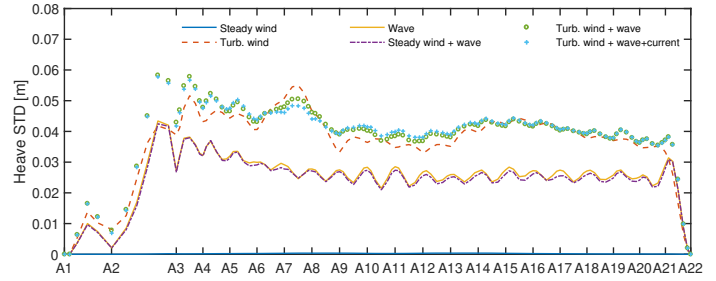(a) Sway
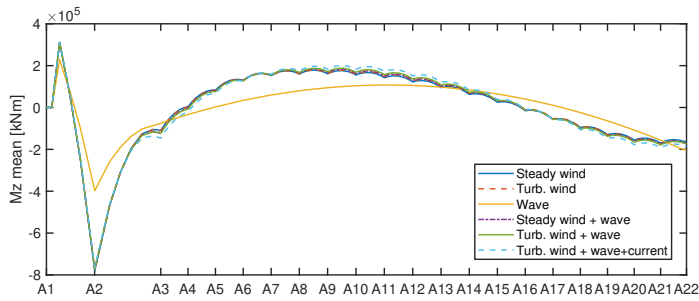
(b) Strong axis bending moment

FIGURE 8. The mean values of (a) sway motion (b) strong axis bending moment along the bridge girder, subjected to different combination of environmental loads.

(a) Heave

(b) Weak axis bending moment, M_y

FIGURE 9. The standard deviations of (a) heave motion (b) weak axis bending moment along the bridge girder, subjected to different combination of environmental loads.

The mean values of heave motion and weak axis bending moment are very close for all six LCs. They are not sensitive to environmental loads. Thus it can be concluded that the mean values of sway motion and strong axis bending moment are mainly induced by wind loads.
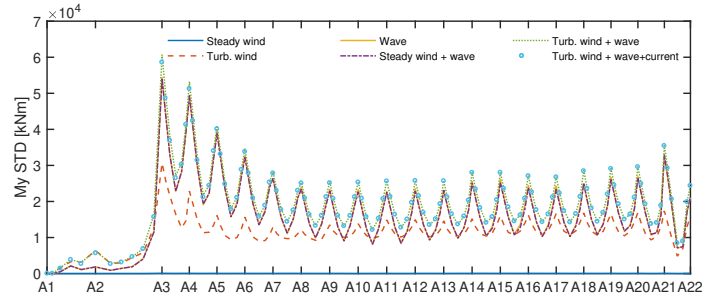
The standard deviations of heave motion and weak axis bending moment along the bridge girder are demonstrated in Fig. 9. The standard deviation of heave motion and weak axis bending moment in cases with waves (LC3, LC4, LC5, LC6) are very close, and much larger than those in cases with wind (LC1, LC2). This indicates that the standard deviation of heave motion and weak axis bending moment are dominated by wave loads.

Fig. 10 shows the standard deviation of sway motion and strong axis bending moment along the bridge girder under different LCs. It can be observed that LC2, LC5 and LC6 have greatly larger standard deviation in sway motion and strong axis bending moment than LC3 and LC4. This is mainly because of turbulent wind. The standard deviations of sway motion and strong axis bending moment are also highly affected by wind loads under cases with turbulent wind.

The sway motion and strong axis bending moment in LC4 with steady wind and waves are generally smaller than those in LC3 with waves. Such reduction is due to aerodynamic damping caused by steady wind. Moreover, aerodynamic damping caused by turbulent wind is much larger than that caused by steady wind. This can be identified by comparing the results in LC2 with tur-
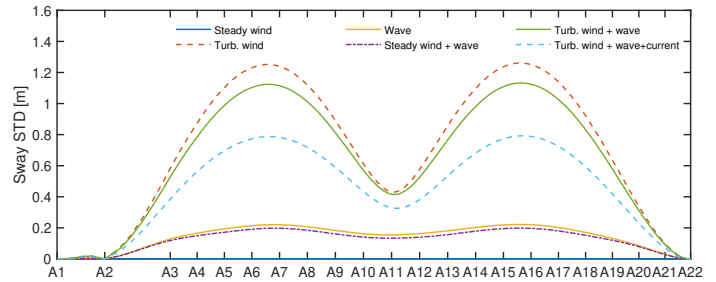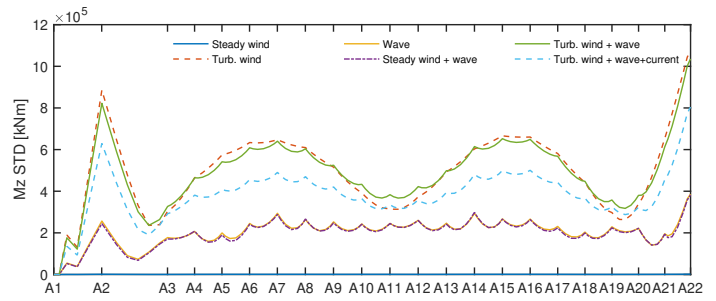

(a) Sway

(b) Strong axis bending moment, M_z

FIGURE 10. The standard deviations of (a) sway motion (b) strong axis bending moment along the bridge girder, subjected to different combination of environmental loads.

bulent wind, LC3 with waves, and LC5 with turbulent wind and waves. With respect to sway motion and strong axis bending moment, the summation of standard deviation in LC2 and LC3 is significantly larger than the standard deviation in LC5.

Comparing results in LC5 and LC6 reveals that current also plays an important role in decreasing the standard deviation of sway motion and strong axis bending moment. This is because current velocity helps to increase the viscous viscous damping effect on the pontoons.

Spectral analysis of dynamic responses

Power spectral analyses are carried out for different responses along the bridge girder in this section. They are used to reveal the difference in contributions of wind, wave and current loads to the variations of dynamic responses.

Fig. 11 presents the power spectra of sway motion at girder nodes at A6 and A11 under different LCs. Variations of sway motion are dominated by low-frequency resonant responses. At A6 it is the first eigen-mode that is mainly excited. However, the second eigen-mode is mainly excited at A11. These low-frequency resonant responses result from low-frequency turbulent wind loads and second-order difference-frequency wave loads. When the turbulent wind and irregular waves are both

considered, the turbulent wind induced resonant responses are more than five times larger than the second-order wave induced resonant responses.

The power spectra of strong axis bending moment of girder nodes at A6 and A11 are shown in Fig. 12. At A6, the power spectrum of strong axis bending moment is mainly dominated by the first eigen-mode resonant response, while at A11 it is mainly dominated by the second eigen-mode resonant response. These low-frequency resonant responses are also due to low-frequency turbulent wind loads and second-order difference-frequency wave loads. Additionally, notable responses are observed between the frequency range of 0.7 to 1.4 rad/s in the power spectrum of strong axis bending moment at A11. By comparing responses from different LCs, these responses are due to wave loads, and they are wave frequency responses and associated resonant responses.

The power spectra of heave motion and weak axis bending moment of girder node at A6 are shown in Fig. 13. The low-frequency responses (below the frequency of 0.5 rad/s) are relatively small compared to these dominant responses in the frequency range of 0.5 to 1.8 rad/s. Moreover, the power spectra of these two responses differ. However, large peaks are observed
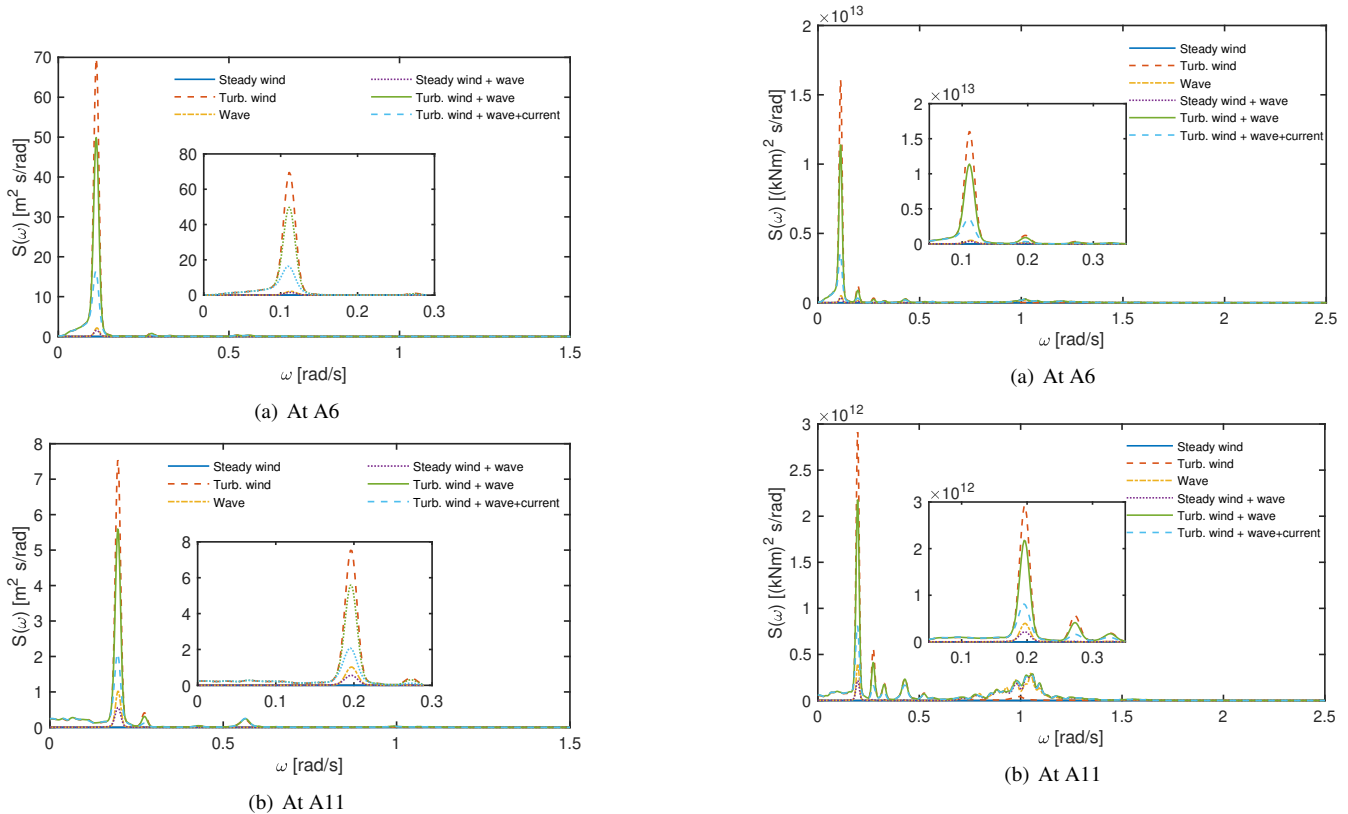
(a) At A6

(b) At A11

FIGURE 11. Power spectra of sway motion of girder nodes at (a) A6, (b) A11 under different combination of environmental loads.

(a) At A6

(b) At A11

FIGURE 12. Power spectra of strong axis bending moment of girder nodes at (a) A6, (b) A11 under different combination of environmental loads.

8

(a) Heave

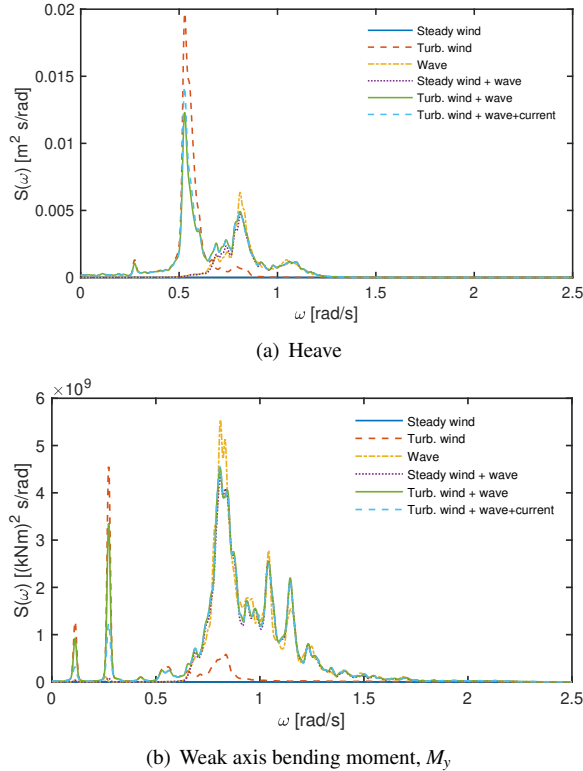(b) Weak axis bending moment, M_y

FIGURE 13. Power spectra of (a) heave motion (b) weak axis bending moment of girder nodes at A6 under different combination of environmental loads.

around the frequency of 0.8 rad/s in the power spectra of heave motion and weak axis bending moment. In the eigen-mode analysis [12], several eigen-modes dominated by vertical motion of the bridge girder are located in the vicinity of 0.8 rad/s, which implies that these large peaks are due to wave-induced resonant responses at these eigen-modes. Peaks are also observed in the power spectra of weak axis bending moment in the frequency range of 0.9 to 1.4 rad/s. These peaks are also because of wave-induced resonant responses.

CONCLUSIONS

This study deals with a study on the wind-, wave-, and current-induced load effects of an end-anchored curved floating bridge. The considered floating bridge, about 4600 m long, was an early concept for crossing Bjørnafjorden. It comprises a cable-stayed high bridge part and a pontoon-supported low bridge part. It also has a number of eigen-modes that might be excited by environmental loads.

A series of numerical simulations are conducted, considering short-crested waves and second-order difference-frequency wave loads, and considering aerodynamic lift, drag and moment on the bridge girder. The main conclusions are as follows:

1. The sway motion and strong axis bending moment along the bridge girder are mainly induced by wind loads.
2. The variations of heave motion and weak axis bending moment are mainly induced by wave loads.
3. Turbulent wind can cause significantly larger low-frequency resonant responses than second-order difference-frequency wave loads.
4. Current loads mainly contribute damping and hence reduce the variations of sway motion and strong axis bending moment.

REFERENCES

[1] Watanabe, E., 2003. "Floating bridges: past and present". *Structural Engineering International,* **13**(2), pp. 128–132.

[2] Hartz, B., 1981. "Dynamic response of the hood-canal floating bridge". In Second ASCE/EMD Specialty conference on dynamic response of structures, Atlanta, GA, USA.

[3] Kvåle, K. A., Sigbjörnsson, R., and Øiseth, O., 2016. "Modelling the stochastic dynamic behaviour of a pontoon bridge: a case study". *Computers & Structures,* **165**, pp. 123–135.

[4] Langen, I., and Sigbjörnsson, R., 1980. "On stochastic dynamics of floating bridges". *Engineering structures,* **2**(4), pp. 209–216.

[5] Watanabe, E., Maruyama, T., Ueda, S., and Tanaka, H., 2015. "Yumemai Floating Swing Arch Bridge of Osaka, Japan". In *Large Floating Structures*. Springer, pp. 61–90.

[6] COWI, 2016. NOT-HYDA-018 Curved bridge navigation channel in south - environmental loading analysis. Report for the Norwegian Public Road Administration. COWI AS, Oslo, Norway.

[7] Løken, A. E., Oftedal, R. A., and Aarsnes, J. V., 1990. "Aspects of hydrodynamic loading and responses in design of floating bridges". In Second symposium on strait crossings, Trondheim, Norway.

[8] Seif, M. S., and Inoue, Y., 1998. "Dynamic analysis of floating bridges". *Marine Structures,* **11**(1), pp. 29 – 46.

[9] Fu, S., Wei, W., Ou, S., Moan, T., Deng, S., and Lie, H., 2017. "A time-domain method for hydroelastic analysis

of floating bridges in inhomogeneous waves". In ASME 2017 36th International Conference on Ocean, Offshore and Arctic Engineering, American Society of Mechanical Engineers.

[10] Lie, H., Fu, S., Fylling, I., Fredriksen, A. G., Bonnemaire, B., and Kjersem, G. L., 2016. "Numerical modelling of floating and submerged bridges subjected to wave, current and wind". In ASME 2016 35th International Conference on Ocean, Offshore and Arctic Engineering, American Society of Mechanical Engineers.

[11] Sha, Y., Amdahl, J., Aalberg, A., and Yu, Z., 2018. "Numerical investigations of the dynamic response of a floating bridge under environmental loadings". *Ships and Offshore Structures*, pp. 1–14.

[12] Cheng, Z., Gao, Z., and Moan, T., 2018. "Hydrodynamic load modeling and analysis of a floating bridge in homogeneous wave conditions". *Marine Structures, 59*, pp. 122–141.

[13] Cheng, Z., Gao, Z., and Moan, T., 2018. "Wave load effect analysis of a floating bridge in a fjord considering inhomogeneous wave conditions". *Engineering Structures, 163*, pp. 197–214.

[14] Cheng, Z., Gao, Z., and Moan, T., 2018. "Numerical modeling and dynamic analysis of a floating bridge subjected wind, wave and current loads". *Submitted for possible publication*.

[15] MARINTEK, 2012. Simo-theory manual version 4.0.

[16] MARINTEK, 2012. Rifelx theory manual, version 4.0.

[17] COWI, 2016. NOT-KTEKA-021 Curve bridge navigation channel in south summary of analyses. Report for the norwegian public road administration. cowi as, oslo, norway.

[18] SVV, 2016. Design basis metocean. Statens Vegnesen, norway.

[19] Lothe, A., and Musch, O., 2015. Bjørnafjorden submerged floating tube bridge: sea state simulations. Tech. rep., Norconsult AS.

[20] Jonkman, B. J., 2009. Turbsim user's guide: Version 1.50. Tech. rep.

[21] Faltinsen, O. M., 1995. *Sea loads on ships and offshore structures*. Cambridge University Press, Cambridge, UK.

[22] Cummins, W. E., 1962. The impulse response function and ship motions. Institut fur Schiffbau, Universitat Hamburg, Hamburg.

[23] DNV GL, 2014. Environmental conditions and environmental loads (DNV-RP-C205). Det Norske Veritas AS, Oslo, Norway.

[24] Strømmen, E., 2010. *Theory of bridge aerodynamics*. Springer Science & Business Media.